CHEMISTRY OF MATERIALS

Article

pubs.acs.org/cm

Atomic Structure and Composition of "Pt_3Co" Nanocatalysts in Fuel Cells: An Aberration-Corrected STEM HAADF Study

Brian Patrick,[†,‡,#] Hyung Chul Ham,[§,▽] Yang Shao-Horn,[∥,⊥] Lawrence F. Allard,[⊗] Gyeong S. Hwang,[§] and Paulo J. Ferreira*[,†]

[†]Materials Science and Engineering Program, [‡]Department of Mechanical Engineering, and [§]Department of Chemical Engineering, University of Texas at Austin, Austin, Texas 78712, United States

[∥]Department of Mechanical Engineering and [⊥]Department of Materials Science and Engineering, Massachusetts Institute of Technology, Cambridge, Massachusetts 02139, United States

[⊗]Materials Science and Technology Division, Oak Ridge National Laboratory, Oak Ridge, Tennessee 37831, United States

Supporting Information

ABSTRACT: Pt_3Co nanoparticles are used to promote the oxygen reduction kinetics and increase the efficiency of proton exchange membrane (PEM) fuel cells. For the first time, aberration-corrected scanning transmission electron microscopy (STEM), STEM image simulations, and DFT calculations are combined to provide insight into the origin of enhanced catalysis of Pt_3Co nanoparticles. Acid-leached nanoparticles exhibit a solid-solution structure but heterogeneous composition, while heat-treated nanoparticles exhibit an ordered structure, except for the first three surface layers where Pt enrichment is observed.

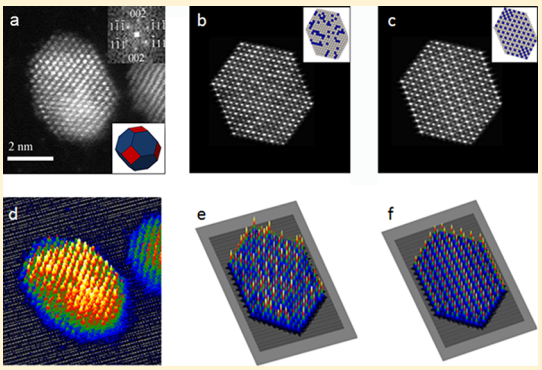

KEYWORDS: *PEM fuel cells, platinum-alloyed catalysts, aberration-corrected STEM, nanoparticles*

INTRODUCTION

Proton exchange membrane fuel cells (PEMFCs) are promising energy conversion devices for transport, stationary and portable applications.[1,2] At the anode side of the PEMFCs, hydrogen fuel is delivered and split into protons and electrons by catalyst nanoparticles (NPs). At the cathode side, air is delivered and the oxygen is catalytically reduced by NPs, where it reacts with the protons crossing the proton exchange membrane, and the electrons travel through the external circuit to form water. The oxygen reduction reaction (ORR) occurring at the cathode has been shown to limit significantly the fuel cell efficiency.[3] In addition, catalyst NPs are typically composed of platinum (Pt), which imposes large costs on PEMFC technology.

Pt-alloy catalysts have been investigated as a replacement for Pt to promote the kinetics of the oxygen reduction reaction (ORR) in the cathode of PEMFCs. Two strategies are shown to increase the intrinsic ORR activity on Pt from studies of extended Pt-alloy surfaces: (1) Pt-segregated surfaces induced by high-temperature annealing[4,5] and (2) Pt-enriched surfaces by acid removal of less noble alloying elements than Pt,[6,8,9] where intrinsic ORR activity (ORR current per true Pt surface area) can increase by 2−10 times relative to that of Pt.[5−12] Combined computational and experimental studies[6,13−16] have shown that the enhanced ORR activity of Pt alloys can be attributed to reduced surface reactivity toward surface oxygenated species as a result of a lower d-band center energy normalized to the Fermi level of Pt alloy surfaces. These developments have motivated research to extend the existing understanding of the ORR mechanism and enhanced activity of bulk Pt-alloy surfaces to nanocatalysts with sizes of practical relevance.

It is well-known that Pt-alloy NP catalysts have ORR activities considerably higher than Pt NPs.[17−22] Pt-alloy NP catalysts can also be subjected to either an acid leaching treatment, which is thought to remove the more reactive alloying elements from the NP surface region,[6,16,23−27] or an annealing step in vacuum or argon to induce surface Pt segregation. More recently, Xin et al.[28] have performed atomic resolution electron energy loss spectroscopy (EELS) analysis on as received NPs, as well as NPs which were subsequently heat-treated and as-received NPs which were heat-treated followed by an acid leaching treatment. The authors[28] showed that there is a Co-free shell on as received NPs, while there is one monolayer Pt shell on {111} facets of NPs which were subjected to a heat treatment after being received. In addition, when the heat-treated NPs were subjected to an acid treatment, the shell thickness grew to around 2.5 monolayers and was independent of facet orientation.

Received: September 10, 2012
Revised: January 18, 2013
Published: January 21, 2013

   dx.doi.org/10.1021/cm3029164 | *Chem. Mater.* 2013, 25, 530−535

In this paper, we have taken a different approach by subjecting a group of as-received "PtCo" alloy NPs with an average atomic ratio of Pt/Co close to 1 first to an acid leaching treatment, and a second group to the same acid leaching procedure, followed by a heat-treatment. As discussed by Chen et al.[23,24] the reason for this is that the acid-treatment produces, for the most part, NPs with a truncated octahedron shape, which is the typical equilibrium shape for Pt NPs, while the subsequent annealing treatment produces a large amount of NPs with a truncated cuboid shape. In terms of ORR activity, acid-leached "Pt_3Co" NPs, show twice the activity of pure Pt NPs, while acid-leached "Pt_3Co" subjected to an additional annealing treatment show an ORR intrinsic activity 4 times that of pure Pt NPs.

However, the near-surface atomic distribution of Pt and Co within individual "Pt_3Co" NPs treated by the above two routes (acid leaching or acid leaching followed high- temperature annealing), which is believed to strongly affect the electronic structure and ORR activity of surface Pt atoms, is still unknown. In addition, there is currently no direct correlation between the atomic distribution and the composition of these NPs (atomic-column by atomic-column basis), particularly on the surface layers, and their catalytic activity. This is mainly due to (1) limitations in the spatial resolution of conventional STEM imaging; (2) the difficulty in separating thickness and mass effects when using high-angular annular dark field (HAADF) STEM imaging; (3) challenges associated with using atomic resolution EELS and energy dispersive spectroscopy (EDS), due to spatial resolution and sample drift and (4) lack of experimental data at the atomic level as input information to theoretical models that may predict the surface reactivity and ORR activity.[29]

In this study, aberration-corrected HAADF STEM imaging, coupled with STEM HAADF simulations, were employed to study the subnanometer-scale distribution of Pt and Co within individual acid-leached or acid-leached and annealed "Pt_3Co" NPs. The combination of these techniques is unique because aberration-corrected HAADF STEM is capable of atomic-column by atomic-column imaging, providing mass−thickness contrast at the atomic level, while the computer simulations allow us to separate the mass and thickness effects and thus determine the local composition of "Pt_3Co" NPs at the atomic scale. In addition, to achieve a fundamental understanding of the near-surface atomic arrangements in "Pt_3Co" NPs and their effect on the ORR activity, density functional theory (DFT) calculations were performed.

METHOD SECTION

Two samples of "Pt_3Co" NPs supported on carbon (Pt 46 wt %) were examined. One was prepared by acid treatment from "PtCo" alloy NPs with an average atomic ratio of Pt/Co close to 1, which was supplied by Tanaka Kikinzoku (TKK) International, Inc. This sample had an average Co atomic percentage of ∼22 atom %.[23,24] The other was obtained by annealing acid-treated-"Pt_3Co" at 1000 K for 3 h at a low pressure of 3×10^{-2} Torr and then cooled in the furnace to 373 K (average heating: 30 K/min; average cooling: 5 K/min).

Both samples were then imaged using a high-resolution JEOL 2010F TEM/STEM located at the University of Texas at Austin, and an aberration-corrected JEOL 2200FS TEM/STEM, equipped with a HAADF detector and located at Oak Ridge National Laboratory. These high-resolution TEM and aberration-corrected STEM images were first analyzed in great detail to create atomic models of the NPs. As shown previously,[23,24] the histograms of 200 randomly selected particles for both the acid-treated and the heat-treated "Pt_3Co" NPs revealed an average particle size of 4 and 5 nm, respectively. In addition, the acid-treatment produced, for the most part, NPs with a truncated octahedron shape (see Supporting Information, Figures S1a and S1b). On the other hand, the annealing treatment produced a large amount of NPs with a truncated cuboid shape (see Supporting Information, Figures S1c and S1d).

From the projected TEM and STEM images and diffraction information, the basic geometries of the NPs were determined. This is important as the STEM simulations depend on crystal orientation and sample thickness. This information was then used in conjunction with the crystal building software, VESTA, to create initial atomic models of the NPs. The atomic models were then exported from VESTA[30] to the HREM Simulation Suite, which is a TEM/STEM simulation software package based on the FFT Multislice technique.[31] The HREM Simulation Suite evaluates both the wave function and its Fourier transform at each slice, using the approximation by Weickenmeier and Kohl,[32] to calculate the elastic scattering amplitude. This is a good approximation when considering electrons scattered at high angles, such as the case of HAADF images.[33,34] The HAADF intensity is then calculated by adding the thermal diffuse scattering factor to the elastic scattering amplitude.[21] This is essential as atomic vibrations dampen the intensity of the electron waves going through the specimen. The microscopy parameters used for the simulations are shown in Table 1.

Table 1. Microscope Parameters Used for the Computer Simulations and Associated with the JEOL 2200 FS Aberration-Corrected STEM Located at Oak Ridge National Laboratory

aperture radius	26 mrad	
defocus	−19.01 Å	
(third order spherical aberration)	1 μm	
(2-fold astigmatism)	1.344 nm	−75.15 deg
(3-fold astigmatism)	39.59 nm	37.1 deg
(4-fold astigmatism)	6.797 μm	−175.35 deg
(5-fold astigmatism)	11.3 μm	46.3 deg
HAADF detector (inner radius)	100 mrad	
HAADF detector (outer radius)	170 mrad	

These parameters correspond to the settings used for the operation of the JEOL 2200FS aberration-corrected STEM at Oak Ridge National Laboratory. The multislice simulations were carried out assuming a step scanning size of 0.18 Å (less than the distance to be resolved), a minimum slice thickness of 1.9 Å (approximately half of the lattice parameter for Pt_3Co), and a Debye−Waller factor of 0.0051 $Å^2$, which is related to the mean square of the thermal displacement of an atom from its equilibrium position, and obtained from X-ray diffraction.[24] After the simulations were completed, the simulated images were compared with the actual images for verification, and the local chemical composition was approximated.

The spin polarized DFT calculations were performed within the generalized gradient approximation (GGA-PW91),[35] as implemented in the Vienna Ab-initio Simulation Package (VASP).[36] The projector augmented wave (PAW) method with a planewave basis set was employed to describe the interaction between core and valence electrons.[37] The valence configurations employed to construct the ionic pseudopotentials are as follows: $5d^{10}\ 6s^1$ for Pt and $3d^8\ 4s^1$ for Co. An energy cutoff of 350 eV was applied for the planewave expansion of the electronic eigenfunctions. For PtCo(100) model surfaces, we constructed nine (and five) atomic-layer slabs with rectangular 2×2 (and 4×4) unit cells where each layer consists of 4 (or 16) atoms. Each slab is separated from its periodic images in the vertical direction by a vacuum space corresponding to seven atomic layers. While the bottom two layers of the nine/five-layer slabs were fixed at corresponding bulk positions, the upper layers were fully relaxed using the conjugate gradient method until residual forces on all the constituent atoms become smaller than 5×10^{-2} eV/Å. For the Brillouin zone integration, we used a $(3 \times 3 \times 1)$ Monkhorst−Pack

dx.doi.org/10.1021/cm3029164 | Chem. Mater. 2013, 25, 530−535

mesh of k points to calculate geometries and total energies, and increased the k-point mesh size up to (11 × 11 × 1) to reevaluate corresponding electronic structures. The lattice constant for bulk Pt is predicted to be 3.98 Å, close to the experimental value of 3.92 Å.

RESULTS AND DISCUSSION

Aberration-corrected HAADF STEM images and respective FFTs of "Pt_3Co" NPs subjected to acid leaching were obtained. A representative example is shown in Figure 1a. The beam direction is [110]. The projection along the aforementioned orientation is important because it confirms that the shape of the NP is a truncated octahedron and allows us to perform accurate computer simulations. In addition, the lack of superlattice reflections in the FFT shows that the NP is not ordered. However, as shown in Figure 1a, the NPs treated by acid leaching show pockets of contrast (bright and dark) throughout the particle. Since the HAADF-STEM contrast is both thickness and atomic number dependent (higher thickness and higher atomic number produce brighter contrast), we have performed computer simulations of the NP exhibiting either a fully ordered Pt_3Co structure (space group $Pm\bar{3}m$) or a random solid-solution (space group $Fm\bar{3}m$), to better understand the variations of contrast. The results are shown in Figures 1(b–c). Figures 1(d–f) show surface plots for the actual image and the simulations where the intensity of the atomic columns can be depicted. Clearly, the experimental image (Figure 1a) does not match the computer simulations of a completely random solid solution or fully ordered NP (Figures 1b–c). Instead, the results show that the acid-leached NP exhibits a solid solution structure but with a heterogeneous composition distribution. This is due to the preferential effect of acid leaching, which tends to remove cobalt from the NP, leaving pockets of Pt-rich concentration. As shown in the Supporting Information, Figure S2, this effect is commonly found in acid-leached NPs.

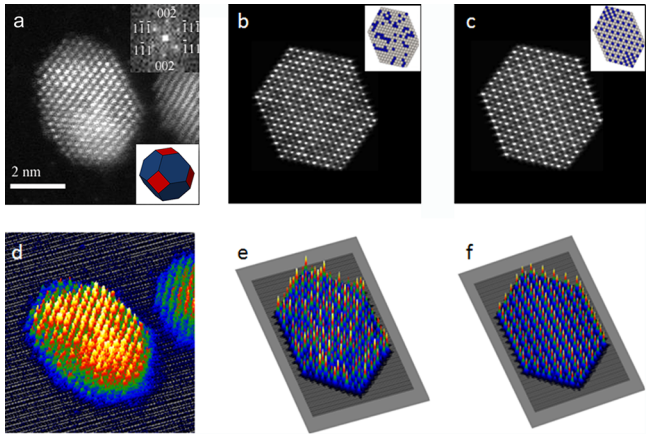

Figure 1. (a) Aberration corrected HAADF STEM image of a truncated octahedron Pt_3Co nanoparticle. The insets show the 3D model and the corresponding FFT. The beam direction is B = [110]. (b) and (c) Computer simulations of the nanoparticle shown in (a), assuming a random solid solution structure (space group $Fm\bar{3}m$) and a fully ordered Pt_3Co structure (space group $Pm\bar{3}m$), respectively. The insets show the corresponding projection of the 3D model. (d), (e), and (f) Surface plots for the actual image, the random solid solution simulation, and the fully ordered simulation, respectively.

Following the same procedure, aberration-corrected HAADF STEM images and respective FFTs of "Pt_3Co" NPs subjected to acid-leaching and annealing were obtained. A representative example is shown in Figure 2a. In this case, the beam direction is [001]. The projection of the NP along the [001] orientation confirms that the NP is a truncated cuboid. Moreover, the NP exhibits an ordered structure throughout (as confirmed by the superlattice {100} type spots shown in the FFT of Figure 2a), except for the first three surface layers where a brighter intensity can be seen. To determine the composition of these three surface layers, the relative intensities of the atomic columns present in these surface layers were measured, and computer simulations to match these relative intensities were performed (Figure 2b and 2c). The simulations represent the case where the truncated cuboid NP is fully ordered from the center to the surface (space group $Pm\bar{3}m$) (Figure 2b), and the case where the truncated cuboid NP shows Pt segregation in the second surface layer (Figure 2c). In the latter simulation, the structure is exactly the same as the case of the fully ordered NP, except for the pure atomic Co columns in the second surface layer, which are substituted by 86% Pt.

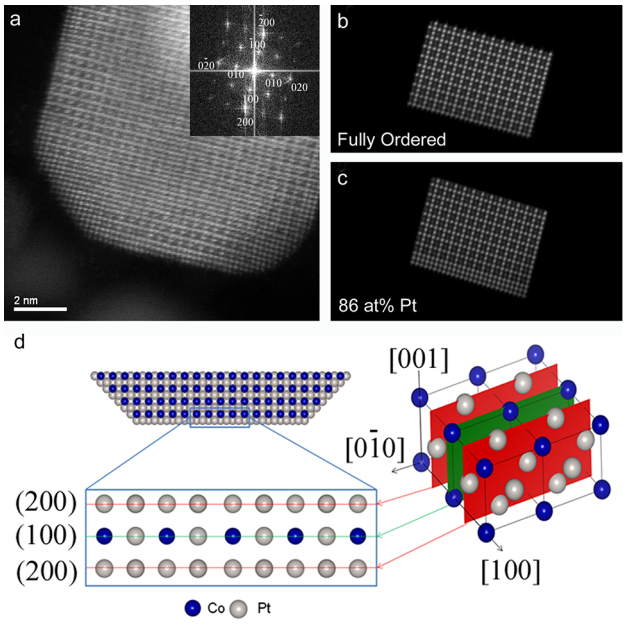

Figure 2. (a) Aberration corrected HAADF STEM image of a truncated cuboid Pt_3Co NP and corresponding FFT (inset). The beam direction is B = [001]. (b) and (c) Computer STEM HAADF simulations of a fully ordered NP and a NP exhibiting 86 atom % Pt on the second surface layer, respectively. (d) Virtual reconstruction of the crystal lattice, assuming a completely ordered structure (space group $Pm\bar{3}m$). In this model, the first and third atomic layers correspond to the {200} type planes, while the second atomic layer corresponds to the {100} type planes.

In this regard, we have first assumed the NP to be fully ordered and observed along the [001] beam direction (Figure 2d). In this case, the projected atomic columns along the {100}-type planes will appear as alternating bright and dark spots, which correspond to pure Pt (bright) and pure Co (dark) columns (Figure 2d). On the other hand, when viewing the {200}-type planes along the [001] beam direction, the contrast should produce a series of uniform bright spots, which correspond to pure Pt columns (Figure 2d). However, as discussed above, the HAADF-STEM contrast is both thickness and atomic number dependent. To separate these two effects, we have further considered that (i) Co is not substituting for Pt on the {200} planes (case of an ideal fully ordered structure)

dx.doi.org/10.1021/cm3029164 | Chem. Mater. 2013, 25, 530–535

and (ii) for sufficiently thin crystals, the HAADF STEM contrast is linearly dependent on thickness.[32,33] On this basis, the variation in intensity of the Pt columns on the {200} planes projected along the [001] direction should be only dependent on thickness when measured along the [100] direction. This procedure allows us to determine the exact geometry of the NP and thus, deconvolute the thickness and atomic number effects. In other words, once we determine the exact shape of the nanoparticle, the simulated intensity of the atomic columns projected along the [001] direction on the {100} and {200} planes, and measured along the [010] direction, should reflect variations in chemical composition only.

For the case of a fully ordered structure, the computer simulated intensity ratio between adjacent atomic columns projected along the [001] direction on the {100} planes and measured along the [010] direction is 2.4. This corresponds to the ratio between columns of pure Pt and the adjacent columns of pure Co (100 atom % Pt÷100 atom % Co) (Figure 2d). On the other hand, for the {200} planes the intensity ratio between adjacent columns of pure Pt is obviously 1 (100 atom % Pt÷100 atom % Pt). The simulation results for the fully ordered case are shown in Figure 2b. When compared with the intensity ratios of the actual HAADF STEM image (Figure 2a) along the same [010] direction and for the same {100} and {200} planes, the computer simulations for a fully ordered NP match well the STEM image, except for the second outmost surface layer (Figure 2b). In fact, the actual STEM image shows a continuous brighter contrast along the second outmost layer (Figure 2a), which reveals a high Pt concentration in this layer.

To quantify the amount of Pt present in the second outmost layer, an intensity profile of the atomic columns projected along the [001] direction on the {100} plane and corresponding to the second outmost surface layer was measured along the [010] direction on the actual STEM image. In this case, the average measured intensity ratio between adjacent columns was found to be 1.2. This ratio is clearly smaller than the 2.4 ratio found for a fully ordered alloy, where a composition of 100 atom % Pt÷100 atom % Co exists between columns of pure Pt and the adjacent columns of pure Co. Thus, the 1.2 ratio confirms the high concentration of Pt on the second outmost layer of the NP, where Pt is substituting for Co along the previously pure Co columns. At this point, several computer simulations were performed, assuming different amounts of Pt and Co along adjacent columns, to match the experimentally observed contrast shown by the second outmost surface layer of the NP. Upon several iterations, the best match was found for an approximate composition of 86% Pt and 14% Co (Figure 2c). This corresponds to a simulated intensity ratio of 1.2 between adjacent atomic columns on the second outmost layer, projected along the [001] direction and measured along the [010] direction; the same value found in the actual HAADF STEM image. The simulations also match a pure Pt composition for the first and third layers. Thus, to a first approximation, the annealed "Pt_3Co" NP shown in Figure 2a has a composition of 100% Pt for the first and third surface layers, while for the second surface layer an approximate composition of 86% Pt and 14% Co was found. Similar examples can be seen in the Supporting Information, Figure S3. We emphasize that these composition values are approximate numbers as the contrast of the STEM images depends on the probe shape, probe size, crystal orientation, thermal scattering factor, defocus and aberration coefficients. For the simulations, we have considered the crystal orientation, thermal scattering factor, defocus and aberration coefficients. However, the probe shape and probe size are not available in the HREM Simulation Suite, and the probe shape is difficult to obtain experimentally.

To better understand the near-surface atomic arrangements of "Pt_3Co" NPs during annealing, particularly on the {100} surfaces, DFT calculations were performed. To start, we calculated the variation in total energy of the Pt−Co system by substituting Pt by 25 atom % Co in one of the first three layers. As shown in Figure 3a, Co atoms prefer to remain in the second surface layer, rather than in the first or third surface layers, where the segregation of Co is unfavorable, as demonstrated by the increase in the overall energy of the system in these layers. With respect to a fully ordered structure, this suggests that the first and third layers prefer to remain 100% Pt, whereas the second layer will experience some sort of composition mix among Pt and Co. To determine the Pt/Co ratio on the second surface layer, we have calculated the variation in the formation energy E_f of Pt−Co alloying with Co content (Figure 3b). The formation energy is given as $E_f = [E_{PtCo} - E_{Pt} + N_{Co}(E_{Pt\text{-}bulk} - E_{Co\text{-}bulk})]/N_{Co}$, where E_{PtCo} and E_{Pt} refer to the total energies of Pt_3Co (100) with and without Co in the second surface layer, respectively, $E_{Pt\text{-}bulk}$ and $E_{Co\text{-}bulk}$ represent bulk Pt and bulk Co energies per atom, respectively, and N_{Co} is the number of Co atoms in the second surface layer. The negative formation energies shown in Figure 3b indicate that Pt−Co alloying is energetically favorable in the second surface layer. A more detailed observation of Figure 3b shows that the formation energy drops steeply and then slowly increases as the Co content increases. According to the cubic spline interpolation based on the calculated data, the minimum

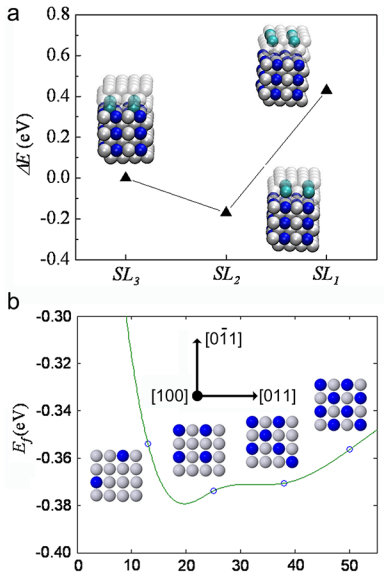

Figure 3. (a) Variation in total energy of the Pt−Co system as a function of composition on the top three surface layers. SL_1, SL_2, and SL_3 represents the cases where the first, second, and third surface layers are composed of 75 atom % Pt: 25 atom % Co, respectively. For each case, the other two surface layers are 100% Pt. The cyan and white spheres indicate Co and Pt atoms in the top three surface layers, while the blue and gray spheres indicate Co and Pt atoms in the fourth and deeper layers. (b) Variation in the formation energy (per Co) of Pt−Co alloying as a function of Co composition on the second surface layer of Pt_3Co (100). In the insets, the blue and light gray spheres indicate Co and Pt atoms, respectively, in the second surface layer.

dx.doi.org/10.1021/cm3029164 | Chem. Mater. 2013, 25, 530−535

value in energy occurs between 13 atom % and 25 atom % Co, which is consistent with the experimental observations of 86 atom % Pt−14 atom % Co found in the STEM images and simulations (Figure 2).

The implications of these results are significant. Figure 4 shows the d-projected density of states (DOS) of surface Pt

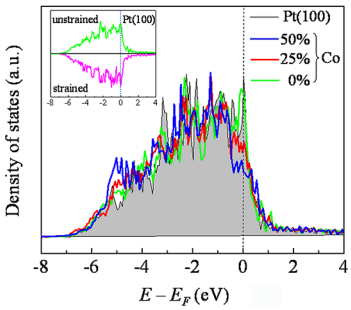

Figure 4. Density of states (DOS) projected on the outmost d-states of surface Pt (5d) atoms as a function of Co content (0%, 25%, and 50%) in the second surface layer of $Pt_3Co(100)$. The DOS for unstrained and strained pure Pt (100) surfaces are also shown in the inset for comparison. The dotted line indicates the Fermi level position.

(5d) atoms for different Co contents in the second surface layer of Pt_3Co (100), as well as for unstrained and strained pure Pt (100) surfaces for comparison. Clearly, as the Co content increases from 0 to 50%, the peak intensity in the higher binding energy regime (-6 eV $< E - E_f < -4$ eV) increases while the peak intensity near the Fermi level (-1 eV $< E - E_f <$ 0 eV) decreases. As a result, there is a noticeable downshift in the Pt d-band center from $\varepsilon_d = -1.69$ eV for unstrained Pt (100) surfaces, to $\Delta\varepsilon_d = 0.21$ eV (50 atom % Co), 0.14 eV (25 atom % Co) and 0.04 eV (0% Co) for Pt_3Co (100), and finally 0.03 eV for strained Pt (100) surfaces. In addition, there is only a slight difference (2.15 atom %) in the surface electronic states between strained Pt (100) surfaces and Pt_3Co (100) with no Co in the top three surface layers. In general, the change of surface electronic structure is apparently attributed to a combination of Pt−Co interaction and compressive strain, imposed by the smaller atomic size of Co. Note that the predicted equilibrium lattice constant of Pt_3Co (space group $Pm\bar{3}m$) is 2.15% smaller than that of pure Pt (space group $Fm\bar{3}m$).

To further understand the effect of Co and strain on the surface reactivity, we calculated the binding energy of atomic O on Pt. For the most preferred bridge site, the O binding strength is predicted to decrease by 0.20 eV (50 atom % Co), 0.17 eV (25 atom % Co), 0.16 eV (0% Co) for the case of Pt_3Co (100), and 0.11 eV for the case of strained Pt (100), when compared with the unstrained Pt (100) surface. The reduced O−Pt binding is likely to result in a rate enhancement of O hydrogenation, which is believed to be the rate-limiting step in the ORR on Pt catalyst.[14] These results strongly support previous experimental observations, where Pt_3Co NPs subjected to an acid leaching treatment followed by annealing exhibited a factor of 4 enhanced activity when compared with pure Pt NPs.[23,24] In other words, during acid leaching, Co atoms are removed from the NP's surface, and the overall surface concentration of Co drops significantly below 50 atom %. However, upon annealing, there is a redistribution of Co from the bulk of the NP toward the second surface layer, leading to a reduced O−Pt binding and thus enhanced activity.

CONCLUSIONS

In summary, we combine for the first time (1) aberration-corrected HAADF STEM imaging, with subnanometer spatial resolution of 0.8 Å and thereby atomic-column by atomic-column imaging; (2) STEM computer simulations, which allow us to separate the mass and thickness effects associated with HAADF STEM imaging and thus determine the local elemental distribution and composition of "Pt_3Co" NPs at the atomic scale; and (3) density functional theory (DFT) calculations, which use the atomic data obtained by HAADF STEM imaging and simulations as input information to calculate fundamental catalytic properties of the nanoparticles. In this work, we show evidence that there is a strong and direct correlation between the specific atomic distribution and composition of the NPs, particularly on the surface layers, and the catalytic activity of NPs, such as Pt_3Co. In particular, we show that "Pt_3Co" NPs obtained from acid leaching exhibit a truncated octahedron shape and form a solid solution of Pt and Co. However, the distribution of Pt and Co is not uniform within individual NPs, with pockets of Pt-rich and Co-rich regions confirmed by experimental and simulated STEM HAADF imaging. Further annealing of the acid-treated "Pt_3Co" NPs leads to the formation of a large number of NPs with a truncated cuboid shape and an ordered structure of Pt and Co (space group $Pm\bar{3}m$). In addition, these annealed "Pt_3Co" NPs tend to exhibit surface segregation in the second outmost surface layer, where an approximate concentration of 86 atom % Pt was found. This is particularly important for the case of {100} surfaces in face-centered-cubic materials, which in the absence of segregation, tend to exhibit high surface energies and thus poor ORR activity. DFT computations confirm that the segregation can be attributed to a combination of Pt−Co interactions and compressive strain, imposed by the smaller Co atoms, while the presence of Co on the second surface layer leads to a reduced O−Pt binding on the surface of these NPs and consequently to a rate enhancement of O hydrogenation and thus greater ORR activity.

ASSOCIATED CONTENT

Supporting Information

Bright-Field TEM images and aberration-corrected STEM images are provided. This material is available free of charge via the Internet at http://pubs.acs.org.

AUTHOR INFORMATION

Corresponding Author

*E-mail: ferreira@mail.utexas.edu.

Present Addresses

[#]Department of Materials Science and Engineering, University of Cailfornia at Berkeley, CA 94720-1760, United States.

[∇]Fuel Cell Research Center, Korea Institute of Science and Technology (KIST), Seoul, 136-791, Republic of Korea.

Notes

The authors declare no competing financial interest.

ACKNOWLEDGMENTS

This work was supported in part by the DOE Hydrogen Initiative program under award number DE-FG02-05ER15728 and the U.S. Department of Energy, Office of Energy Efficiency

and Renewable Energy, Fuel Cell Technologies Program through Argonne National Laboratory under contract DE-AC02-06CH11357. This research at the Oak Ridge National Laboratory's High Temperature Materials Laboratory was sponsored by the U.S. Department of Energy, Office of Energy Efficiency and Renewable Energy, Vehicle Technologies Program. G.S.H also acknowledges partial support under R.A. Welch Foundation Grant F-1535.

REFERENCES

(1) Steele, B.; Heinzel, A. *Nature* **2001**, *414*, 345−352.
(2) Nogami, M.; Miyamura, K.; Abe, Y. *J. Electrochem. Soc.* **1997**, *144* (6), 2175.
(3) Gasteiger, H. A.; Kocha, S. S.; Sompalli, B.; Wagner, F. T. *Appl. Catal., B* **2005**, *56*, 9.
(4) Gauthier, Y. *Surf. Rev. Lett.* **1996**, *3*, 1663.
(5) Ruban, A. V.; Skriver, H. L.; Norskov, J. K. *Phys. Rev. B* **1999**, *59*, 15990.
(6) Stamenkovic, V. R.; Mun, B. S.; Mayrhofer, K. J. J.; Ross, P. N.; Markovic, N. M. *J. Am. Chem. Soc.* **2006**, *128*, 8813.
(7) Stamenkovic, V. R.; Fowler, B.; Mun, B. S.; Wang, G. F.; Ross, P. N.; Lucas, C. A.; Markovic, N. M. *Science* **2007**, *315*, 493.
(8) Toda, T.; Igarashi, H.; Uchida, H.; Watanabe, M. *J. Electrochem. Soc.* **1999**, *146*, 3750.
(9) Stamenkovic, V. R.; Mun, B. S.; Arenz, M.; Mayrhofer, K. J. J.; Lucas, C. A.; Wang, G. F.; Ross, P. N.; Markovic, N. M. *Nat. Mater.* **2007**, *6*, 241.
(10) Stamenkovic, V.; Schmidt, T. J.; Ross, P. N.; Markovic, N. M. *J. Electroanal. Chem.* **2003**, *554*, 191.
(11) Paulus, U. A.; Wokaun, A.; Scherer, G. G.; Schmidt, T. J.; Stamenkovic, V.; Radmilovic, V.; Markovic, N. M.; Ross, P. N. *J. Phys.Chem. B* **2002**, *106*, 4181.
(12) Stamenkovic, V.; Schmidt, T. J.; Ross, P. N.; Markovic, N. M. *J. Phys. Chem. B* **2002**, *106*, 11970.
(13) Norskov, J. K.; Rossmeisl, J.; Logadottir, A.; Lindqvist, L.; Kitchin, J. R.; Bligaard, T.; Jonsson, H. *J. Phys. Chem. B* **2004**, *108*, 17886.
(14) Stamenkovic, V.; Mun, B. S.; Mayrhofer, K. J. J.; Ross, P. N.; Markovic, N. M.; Rossmeisl, J.; Greeley, J.; Norskov, J. K. *Angew. Chem., Int. Ed.* **2006**, *45*, 2897.
(15) Xu, Y.; Ruban, A. V.; Mavrikakis, M. *J. Am. Chem. Soc.* **2004**, *126*, 4717.
(16) Greeley, J.; Norskov, J. K. *Electrochim. Acta* **2007**, *52*, 5829.
(17) Paulus, U. A.; Wokaun, A.; Scherer, G. G.; Schmidt, T. J.; Stamenkovic, V.; Radmilovic, V.; Markovic, N. M.; Ross, P. N. *J. Phys. Chem. B* **2002**, *106*, 4181−4191.
(18) Watanabe, M.; Tsurumi, K.; Mizukami, T.; Nakamura, T.; Stonehart, P. *J. Electrochem. Soc.* **1994**, *141*, 2659−2668.
(19) Mukerjee, S.; Srinivasan, S. *J. Electroanal. Chem.* **1993**, *357*, 201−224.
(20) Mukerjee, S.; Srinivasan, S.; Soriaga, M. P.; Mcbreen, J. *J. Phys. Chem.* **1995**, *99*, 4577−4589.
(21) Koh, S.; Strasser, P. *J. Am. Chem. Soc.* **2007**, *129*, 12624.
(22) Mukerjee, S.; Srinivasan, S.; Soriaga, M. P.; Mcbreen, J. *J. Electrochem. Soc.* **1995**, *142*, 1409−1422.
(23) Chen, S.; Ferreira, P. J.; Sheng, W.; Yabuuchi, N.; Allard, L. F.; Shao-Horn, Y. *J. Am. Chem. Soc.* **2008**, *130*, 13818−13819.
(24) Chen, S.; Sheng, W.; Yabuuchi, N.; Ferreira, P. J.; Allard, L. F.; Shao-Horn, Y. *J. Phys. Chem. C* **2009**, *113*, 1109−1125.
(25) Lai, F.; Su, W.; Sarma, L.; Liu, D.; Hsieh, C.; Lee, J.; Hwang, B. *Chem.—Eur. J.* **2010**, *16*, 4602−4611.
(26) Oezaslan, M.; Heggen, M.; Strasser, P. *J. Am. Chem. Soc.* **2011**, *134*, 514−524.
(27) Heggen, M.; Oezaslan, M.; Houben, L.; Strasser, P. *J. Phys. Chem. C* **2012**, *116*, 19073−19083.
(28) Xin, H.; Mundy, J.; Liu, Z.; Cabezas, R.; Hovden, R.; Kourkoutis, L.; Zhang, J.; Subramanian, N.; Makharia, R.; Wagner, F.; Muller, D. A. *Nano Lett.* **2012**, *12* (1), 490−497.
(29) Schlapka, A.; Lischka, M.; Groß, A.; Käsberger, U.; Jakob, P. *Phys. Rev. Lett.* **2003**, *91*, 016101.
(30) Momma, K.; Izumi, F. *J. Appl. Crystallogr.* **2008**, *41*, 653−658.
(31) Ishizuka, K. *Ultramicroscopy* **2001**, *90*, 71−83.
(32) Weickenmeier, A.; Kohl, A. *Acta Crystallogr.* **1991**, *A47*, 590−603.
(33) Dinges, C.; Berger, A.; Rose, H. *Ultramicroscopy* **1995**, *60*, 49−70.
(34) Dinges, C.; Rose, H. *Scanning Microsc.* **1997**, *11*, 277−286.
(35) Perdew, J. P.; Wang, Y. *Phys. Rev. B* **1992**, *45*, 13244−13249.
(36) Kresse, G.; Furthmuller, J. *VASP the guide*; Vienna University of Technology: Vienna, Austria, 2001.
(37) Blochl, P. E. *Phys. Rev. B* **1994**, *50*, 17953−17979.